

Supplementary Information

Unraveling the Structural and Morphological Stability of Oxygen Vacancy Engineered Leaf-Templated CaTiO₃ towards Photocatalytic H₂ Evolution and N₂ Fixation Reactions

Ashish Kumar,¹ Manish Kumar,² Vempuluru Navakoteswara Rao,³

Muthukonda Venkatakrisnan Shankar,³ Saswata Bhattacharya,^{2*} and Venkata Krishnan^{1*}

¹School of Basic Sciences and Advanced Materials Research Center, Indian Institute of Technology Mandi, Kamand, Mandi 175075, Himachal Pradesh, India.

²Department of Physics, Indian Institute of Technology Delhi, New Delhi 110016, India.

³Nanocatalysis and Solar Fuels Research Laboratory, Department of Materials Science & Nanotechnology, Yogi Vemana University, Kadapa 516005, Andhra Pradesh, India.

*Corresponding authors: saswata@physics.iitd.ac.in and ykn@iitmandi.ac.in

Sl. No.	Content	Pg. No.
1	Materials characterization, photoelectrochemical study and computational details	S-2
2	O-1s XPS spectra of DCT4	S-6
3	FESEM images of DCT3	S-7
4	BET surface area of CT and DCT3	S-8
5	DRS, REELS and VB XPS spectra	S-9
6	PXRD, TEM, Elemental mapping and EDAX spectra of DCT3c	S-10
7	XPS spectra of DCT3c	S-11
8	FESEM images of DCT3 and DCT3c after ultrasonication and stirring process	S-12
9	FESEM images, EDAX and Elemental mapping of recycled DCT3c	S-13
10	PXRD patterns and O-1s XPS spectra of recycled DCT3c	S-14
11	N-1s XPS spectra of CT and DCT3	S-15
12	Time-dependent UV-vis absorption plots for NH ₃ formation	S-16
13	Calibration curve for NH ₃ quantification	S-17
14	PL, photocurrent and impedance spectra of CT and DCT3	S-18
15	Mechanism illustration of photocatalytic H ₂ evolution and N ₂ fixation over oxygen vacancy engineered CaTiO ₃	S-19

16	STH efficiency calculation	S-20
17	Comparison of H ₂ evolution performance of oxygen vacancy engineered leaf-templated CaTiO ₃ with other similar materials	S-21
18	Summary of photocatalytic N ₂ fixation results	S-22
19	Comparison of N ₂ fixation performance of oxygen vacancy engineered leaf-templated CaTiO ₃ with other similar materials	S-23
20	References	S-24

Materials characterizations

The phase purity and structural properties of prepared samples was investigated by using powder x-ray diffraction (PXRD) recorded on a Rigaku Smart Lab 9 kW rotating anode diffractometer working in Bragg configuration with Ni-filtered Cu K_{α} irradiation ($\lambda = 0.1542$ nm) at 45 kV and 100 mA. The PXRD patterns were collected from a 2θ range of 5–90° with a scan rate of 2° per minute. Agilent K8002AA Carry 660 instrument was used for functional group analysis by FTIR measurements. Morphology of the as prepared samples was investigated by using field emission scanning electron microscopy (SEM) FEI Nova Nano SEM-450 instrument. Transmission electron microscopy (TEM) and high resolution TEM (HRTEM) images were recorded on a Technai G 20 (FEI) S-twin microscope operating at 200 kV (accelerating voltage). The spatial distribution and presence of constituent elements in the prepared samples were studied by elemental mapping and EDAX spectroscopy facilities attached with the above mentioned TEM instrument. X-ray photoelectron spectroscopy (XPS) measurements were performed on a ThermoFisher Scientific NEXSA photoelectron spectrometer with Al $K_{\alpha\alpha}$ (1486.6 eV) dual anode as the source, operating at a 12 kV anode voltage and 6.50 mA filament current. The XPS data were collected with a pass energy of 50 eV at 9×10^{-8} mbar vacuum and analysis of the obtained data was performed using Avantage software. Reflected electron energy loss spectroscopy (REELS) measurements were carried to measure the band gap of the materials and were performed on materials palette. The optical absorbance and reflectance of the resultant samples were measured by diffuse reflectance spectroscopy (DRS) on a Perkin Elmer UV-visible-NIR Lambda 750 spectrophotometer using polytetrafluoroethylene (PTFE) polymer as diffuse reflectance standard. Photoluminescence (PL) spectra were acquired on Agilent Technologies Cary Eclipse fluorescence spectrophotometer. The Brunauer-Emmett-Teller (BET) surface area studies were carried out at 77 K on Quantachrome Autosorb-iQ-MP-XR system. The photoelectrochemical measurements were carried out by using a scanning potentiostat (Metrohm, Autolab).

Photoelectrochemical study

The photocurrent and impedance of control CT and best DCT3 samples were measured by using a standard three-electrode system 150 W UV light lamp. The working electrodes were prepared by depositing the photocatalysts on a FTO substrate in 1

cm² surface area and 0.1 M Na₂SO₄ aqueous solution was used as an electrolyte. Platinum wire and Ag/AgCl electrode were used as counter and reference electrodes, respectively. For the preparation of catalyst ink, 5 mg of catalyst was mixed with 200 μL of DI water, 200 μL of isopropyl alcohol (IPA) and 20 μL of Nafion solution was added as a binder followed by ultrasonication process. The transient photocurrent measurements were performed at a potential of 0 V and Nyquist plots were examined in the frequency range from 0.1 to 10⁵ Hz.

Computational details

The spin-polarized density functional theory (DFT)¹⁻² calculations have been performed by employing Vienna *Ab Initio* Simulation Package (VASP).³⁻⁴ The electron-ion interactions have been considered by using projector augmented wave (PAW)⁴⁻⁵ pseudopotentials for each species (viz. Ca, Ti, O, N and H). All the structures are optimized (only atomic positions) using PBE⁶ exchange-correlation (xc) functional. The geometries are optimized until the Hellmann-Feynman forces acting on atoms are smaller than 0.001 eV/Å. The self-consistency loop has been converged with an energy threshold of 0.01 meV. The single-point energy calculations have been carried out using HSE06⁷ xc functional with exact Fock exchange parameter of 18% (Note that the default 25% exact Fock exchange parameter overestimated the band gap. It yields a band gap of 3.95 eV). The 2 x 2 x 1 supercell (80-atom) has been used to carry out the calculations, so that the defects get fully localized into the systems. The *k*-mesh of 4 x 4 x 6 generated using Monkhorst-Pack⁸ scheme has been used for Brillouin zone sampling while optimization. The *k*-mesh of 2 x 2 x 3 has been used for single-point energy calculations. An energy cutoff of 500 eV has been used for plane-wave basis set expansion.

Further, for N₂ fixation, the CaTiO₃ (001) surfaces with CaO- and TiO₂-termination have been modeled as (2x2) supercell with a periodic 4-layer wherein the lower two layers are fixed and the upper two layers are relaxed. A vacuum thickness of 15 Å has been used in order to eliminate the interaction between the periodic slabs. The *k*-mesh of 2 x 2 x 1 has been used for single-point energy calculations of the surfaces. The Gibbs free energy of formation (ΔG) for H adsorption is calculated as follows:

$$\Delta G = E_{surf+H} - E_{surf} - \frac{E_{H_2}}{2} + \Delta E_{ZPE} - T\Delta S$$

Where E_{surf+H} and E_{surf} are the total energies of surface with and without H adsorbates, respectively. E_{H_2} is the total energy of H_2 molecule. ΔE_{ZPE} is the difference in zero point energy between the adsorbed and the gas phase, T is the temperature and ΔS is the change in entropy. The vibrational energies of the species determine the ΔE_{ZPE} and ΔS . For creating a single O-vacancy at CaO-terminated and TiO_2 -terminated surfaces, we have scanned different positions and found out the minimum energy configuration. Subsequently, the N_2 has been adsorbed at the defected site. Further, the hydrogenation is taken into account for N_2 fixation.

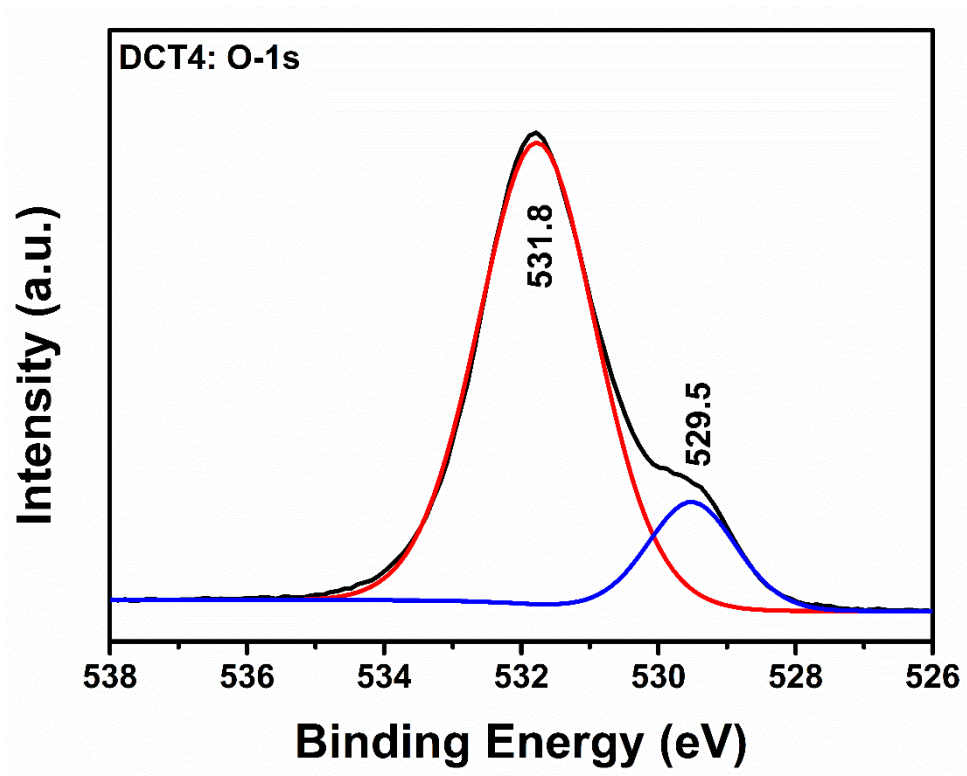


Figure S1. O-1s XPS spectra of DCT4.

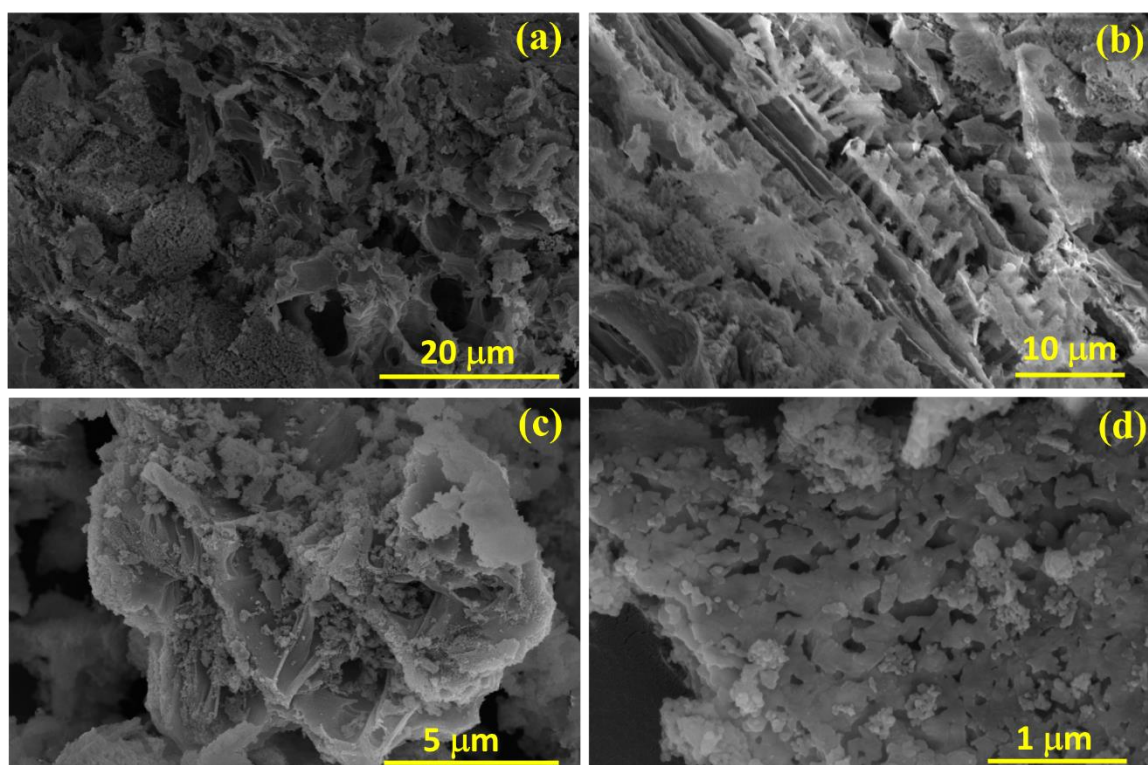


Figure S2. (a-d) FESEM images of DCT3 sample showing the partial destruction of morphology.

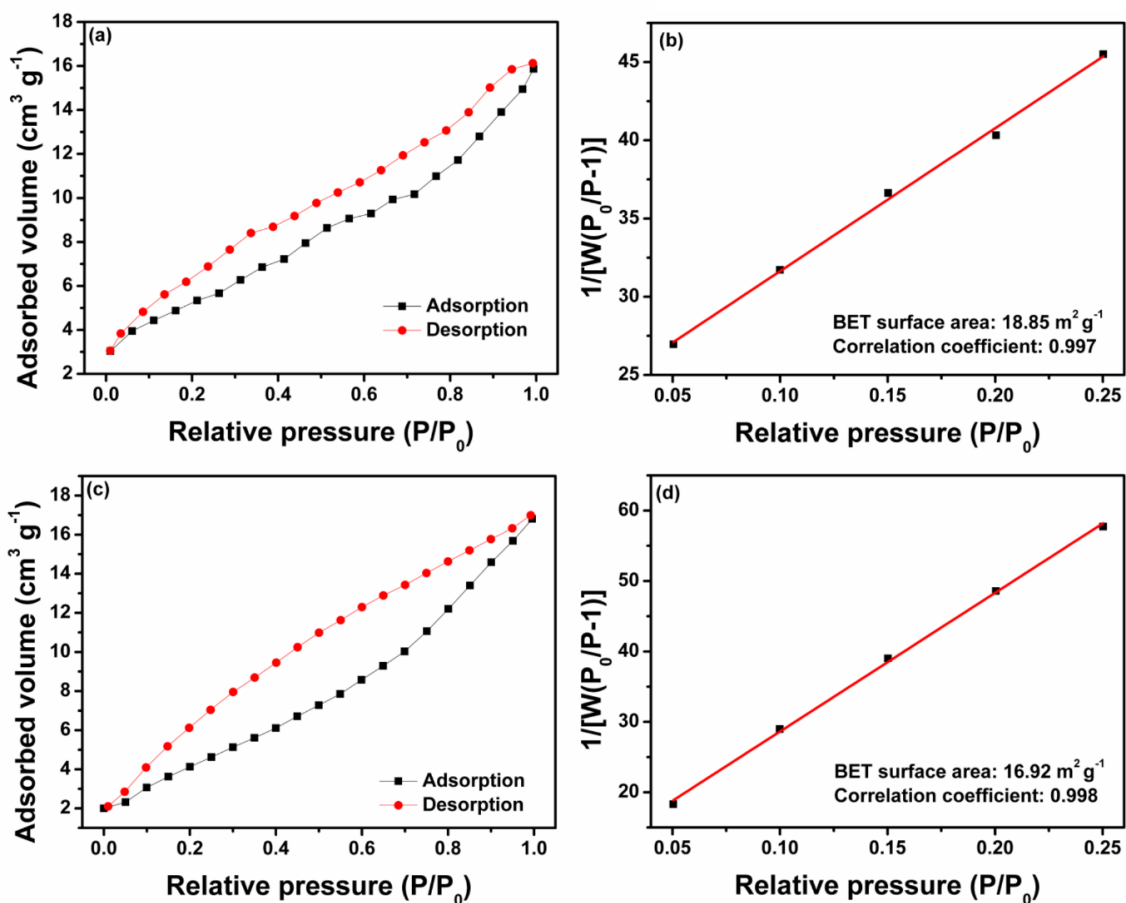


Figure S3. N₂ adsorption-desorption isotherms and BET surface area of (a, b) CT and (c, d) DCT3.

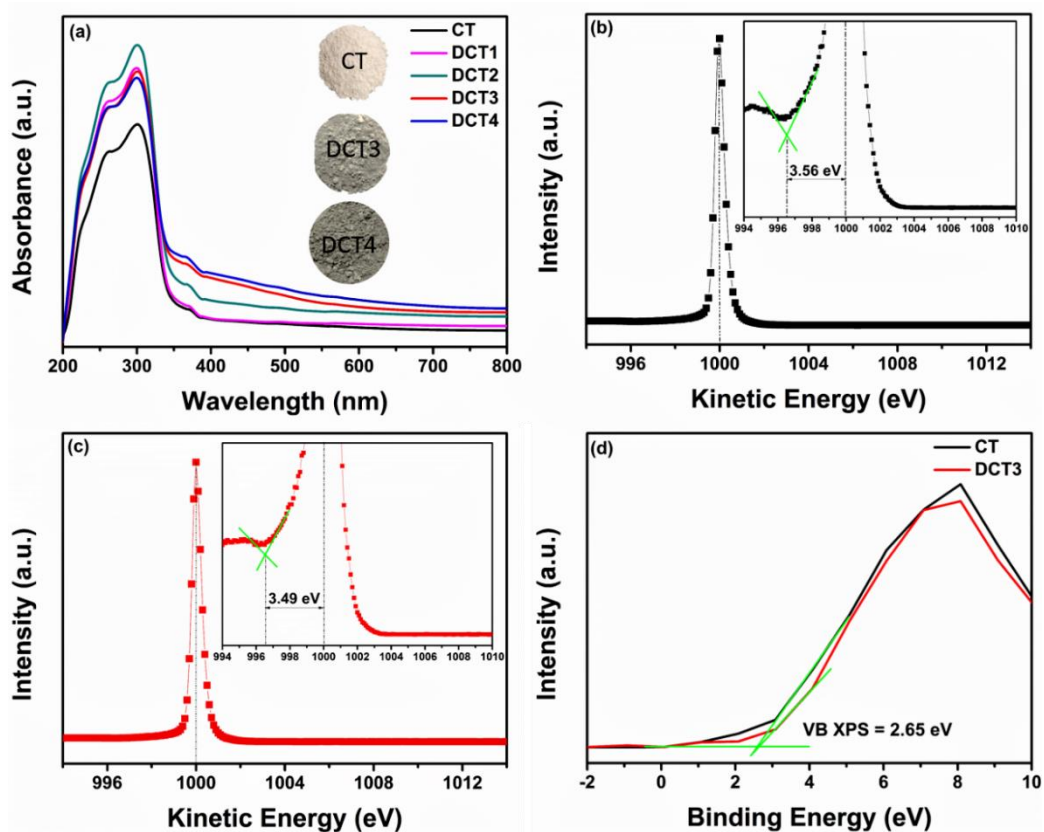


Figure S4. (a) DRS spectra of CT and different DCT materials (inset shows the color of different materials), (b, c) REELS spectra of CT and DCT3 and (d) XPS VB spectra of CT, DCT3 and DCT4 materials.

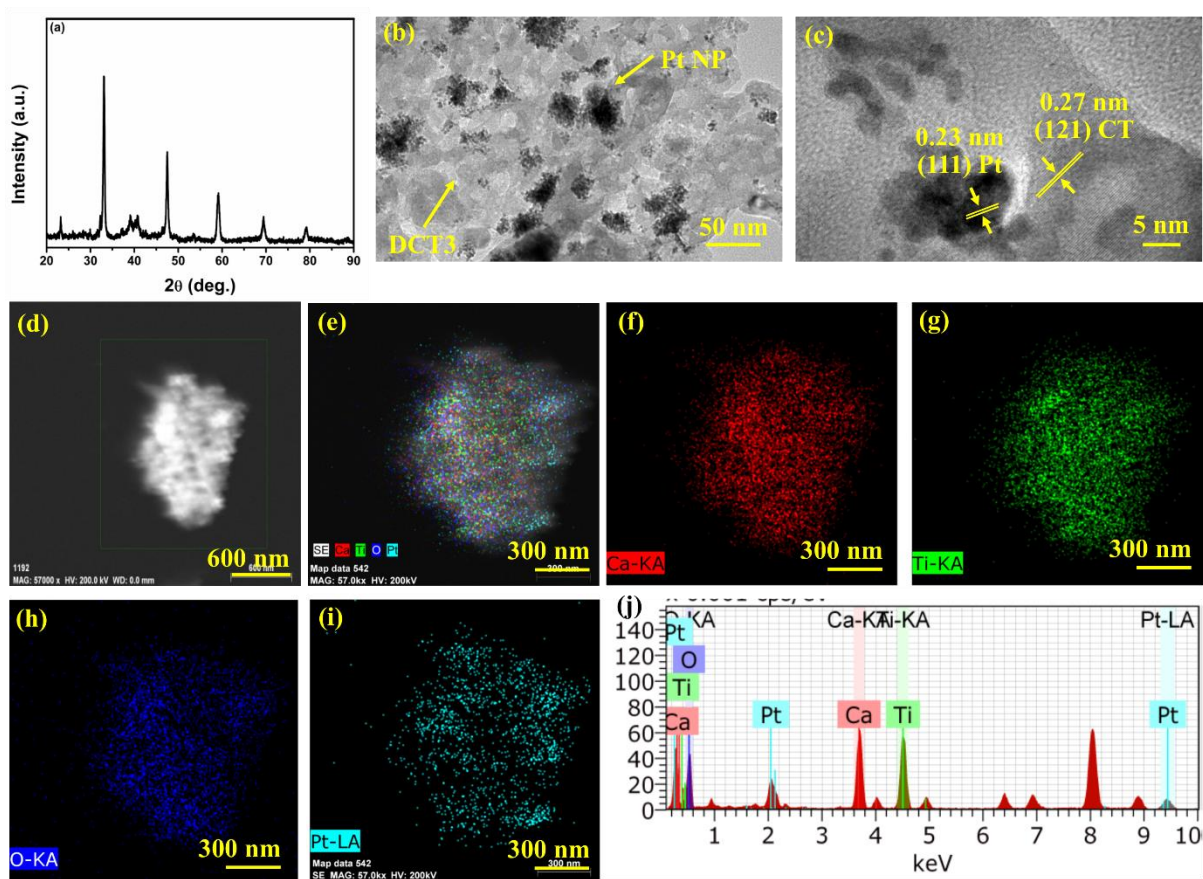


Figure S5. (a) PXRD patterns of DCT3c material, (b, c) TEM and HRTEM images, (d-i) elemental mapping and (j) EDAX spectra of DCT3c showing the presence of Pt nanoparticles.

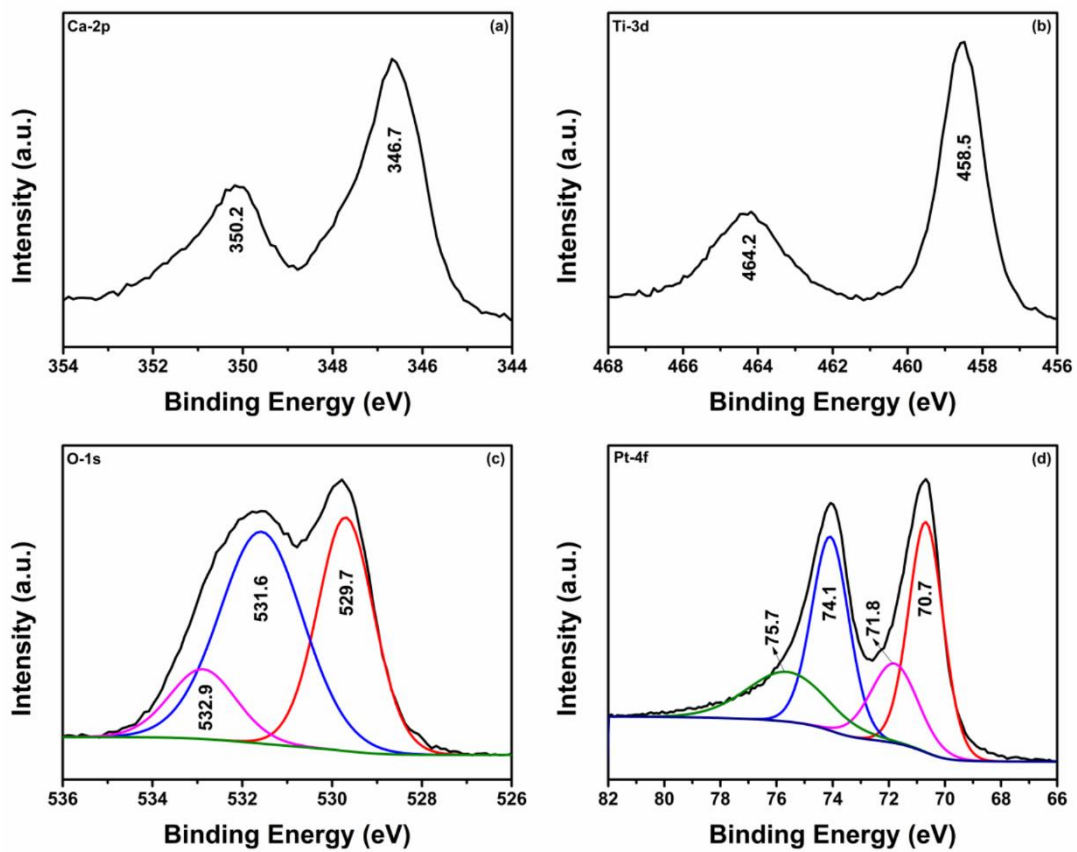


Figure S6. XPS spectra of DCT3c material (a) Ca-2p, (b) Ti-3d, (c) O-1s and (d) Pt-4f.

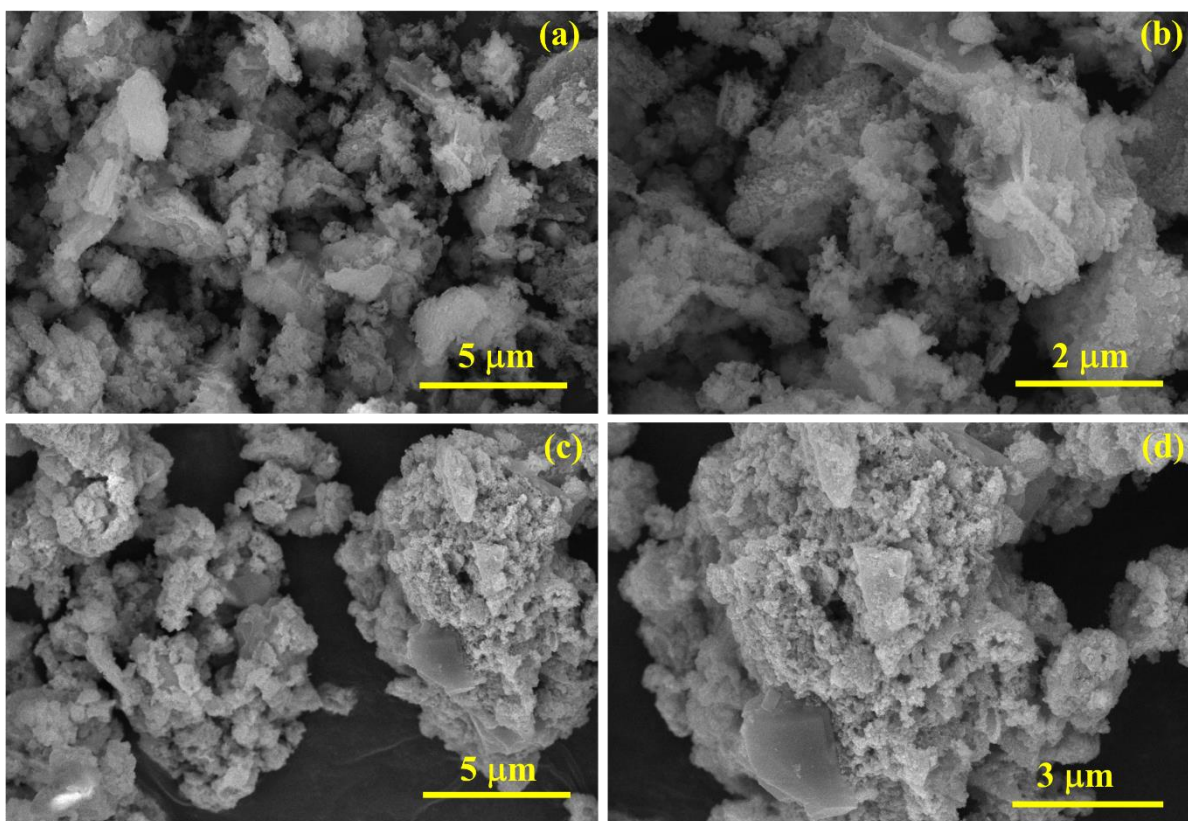


Figure S7. FESEM images of (a, b) DCT3 and (c, d) DCT3c samples after ultrasonication and stirring process.

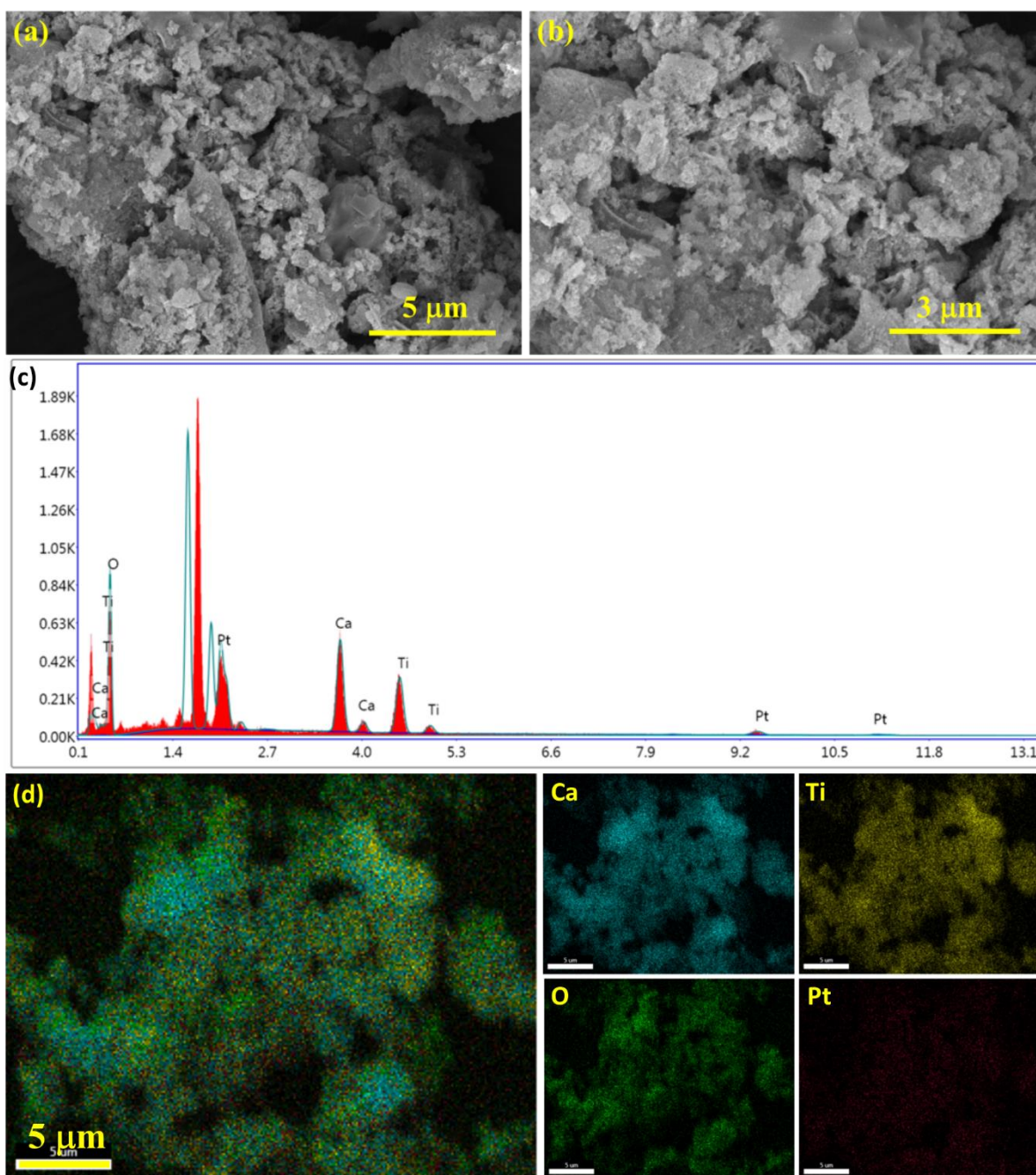


Figure S8. (a, b) FESEM images, (c) EDAX and (d) elemental mapping of recycled DCT3c.

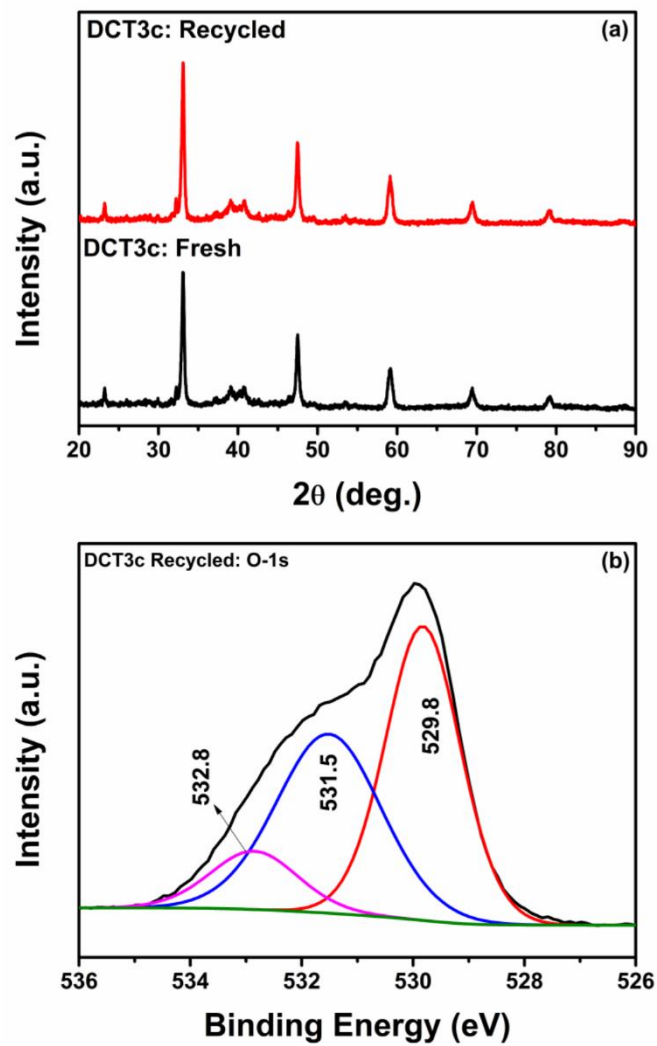


Figure S9. (a) PXR D patterns of fresh and recycled DCT3c and (b) O-1s XPS spectra of recycled DCT3c.

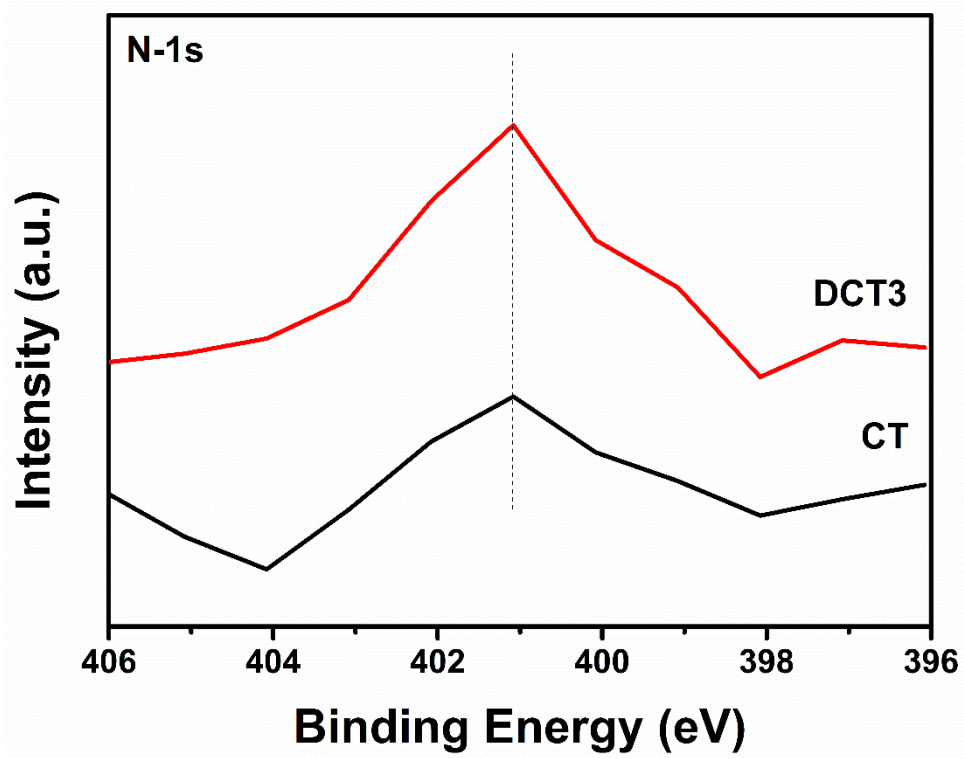


Figure S10. N-1s XPS spectra of CT and DCT3.

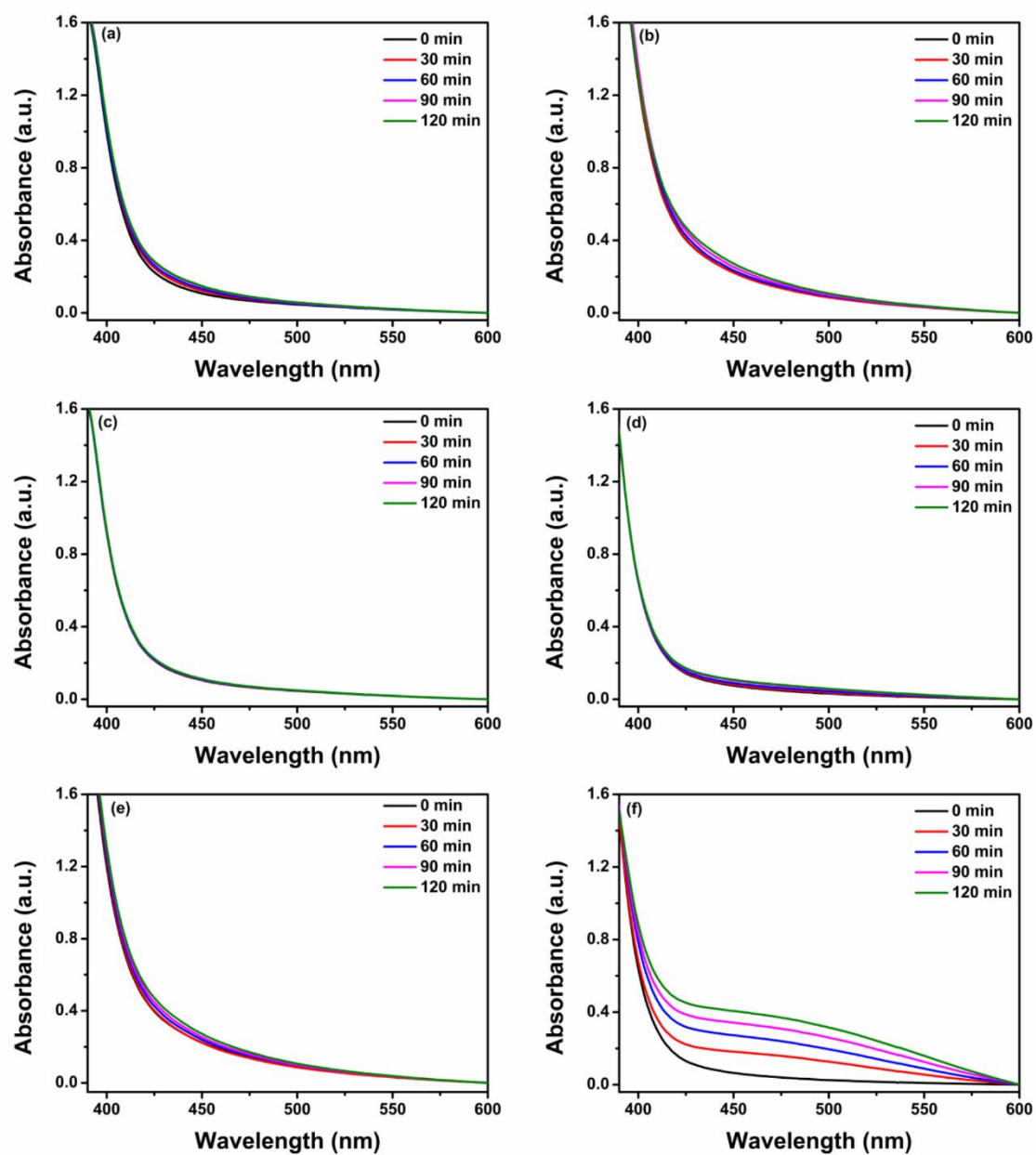


Figure S11. Time-dependent UV-vis absorption plots for NH_3 formation over (a) CT and (b) DCT3 in pure water reaction condition; (c) CT and (d) DCT3 in Ar atmosphere and 1 vol.% aqueous methanol and (e) CT and (f) DCT in N_2 atmosphere and 1 vol.% aqueous methanol.

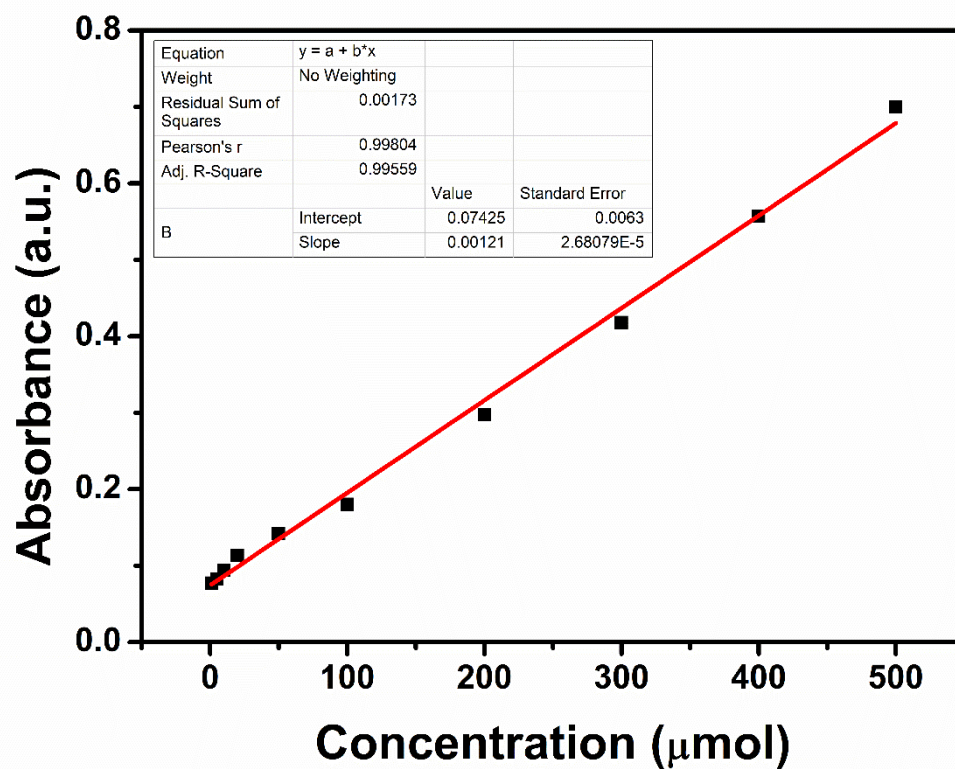


Figure S12. Calibration curve for NH₃ quantification obtained from absorbance vs standard NH₄Cl solution concentration.

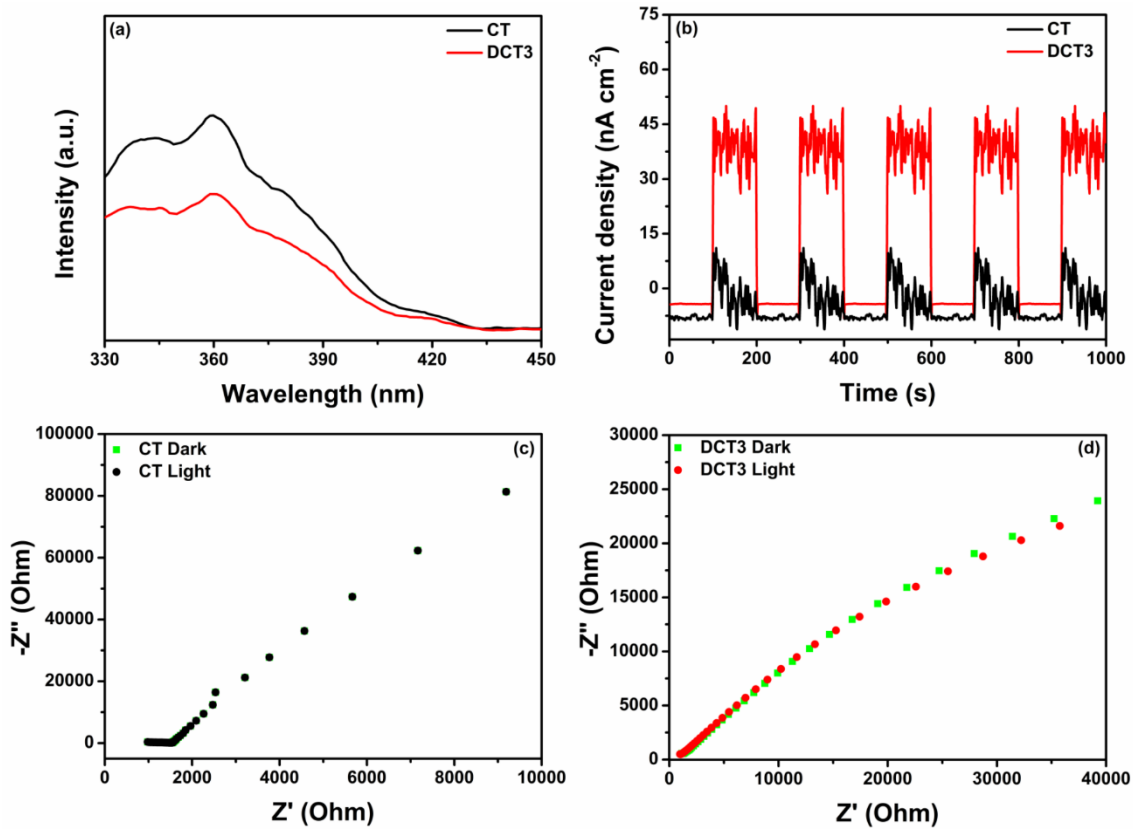


Figure S13. (a) Photoluminescence, (b) photocurrent and (c, d) impedance spectra of CT and DCT3 samples.

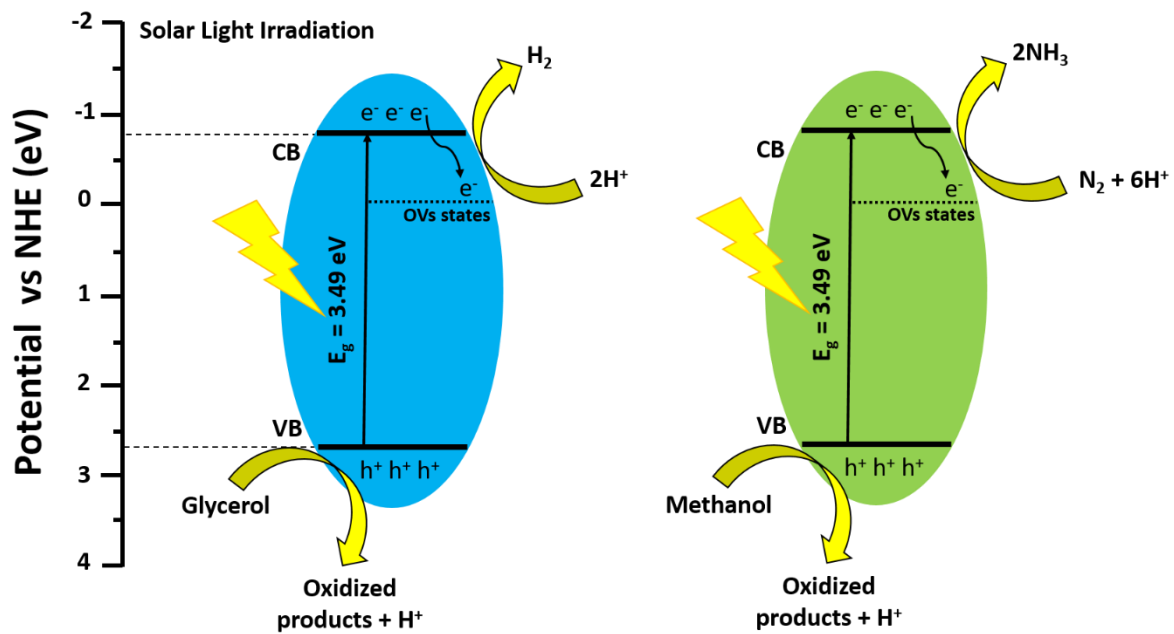


Figure S14. Mechanism illustration of photocatalytic H₂ evolution and N₂ fixation over oxygen vacancy engineered CaTiO₃ (DCT3).

Solar to hydrogen conversion efficiency

The solar to H₂ conversion efficiency (STH) was calculated by using the following formula

$$\text{STH} = \frac{\text{output energy as H}_2 / \text{J}}{\text{The energy density of incident Solar light/ J cm}^{-2} \times \text{irradiated area cm}^2} \times 100$$
$$= \frac{\Delta G (\text{H}_2\text{O})/\text{J mol}^{-1} \times \text{Rate of H}_2 \text{ production } (\mu\text{mol. h}^{-1} \cdot \text{g}^{-1})}{3600 \times \text{Solar light energy/mW cm}^{-2} \times \text{irradiated area cm}^2}$$

Here, Gibbs free energy (ΔG) for H₂O = 237 KJ mol⁻¹

Time (h) = 1 h (3600 sec)

Solar light energy density measured by power meter = 328 mW cm⁻²

Irradiation area (cm²) = 33

Rate of H₂ production = 3418.0 $\mu\text{mol. h}^{-1} \cdot \text{g}^{-1}$

$$\text{STH} = \frac{237 \times 3418}{3600 \times 328 \times 33} \times 100$$

$$= \frac{810,066}{38,966,400} \times 100$$

$$= 0.0207 \times 100$$

$$\text{STH} = 2.07\%$$

Table S1. Comparison of H₂ evolution performance of oxygen vacancy engineered leaf-templated CaTiO₃ with other similar materials. (OVs means oxygen vacancies)

Photocatalyst	Cocatalyst used	Sacrificial agent	Light source	H ₂ evolved	STH	Ref. (Year)
Hydrogenated CaTiO ₃ (OVs)	Pt	Methanol	300 W Xe lamp (AM 1.5G filter)	2.3 mmol g ⁻¹ h ⁻¹	-	⁹ (2020)
SrTiO ₃ (OVs)	Pt	Methanol	UV-visible light	2.2 mmol g ⁻¹ h ⁻¹	-	¹⁰ (2014)
SrTiO ₃ with bulk Ti ³⁺ defects	Pt	Methanol	300 W Xe lamp	311.8 μmol h ⁻¹	-	¹¹ (2016)
TiO ₂ (OVs)	Pt	Methanol	300 W Xe lamp	114.9 μmol g ⁻¹ h ⁻¹	-	¹² (2019)
Mn-loaded ZnO (OVs)	Not used	Methanol	150 W metal halide lamp	70.0 μmol g ⁻¹ h ⁻¹	-	¹³ (2015)
g-C ₃ N ₄ -ZnO (OVs)	Pt	TEOA	300 W Xe lamp (λ >420 nm)	322.0 μmol g ⁻¹ h ⁻¹	-	¹⁴ (2017)
CdS/ZnO (OVs)	Not used	Na ₂ SO ₃ and Na ₂ S	300 W Xe lamp	132.9 μmol h ⁻¹	-	¹⁵ (2017)
CaTiO ₃ (OVs)	Not used Pt	Glycerol	260 W Xe lamp (AM 1.5G filter)	762.2 μmol h ⁻¹ g ⁻¹ 2.4 mmol h ⁻¹ g ⁻¹	- 2.07%	This work

Table S2. Summary of photocatalytic N₂ fixation results.

Catalyst and gas used	Reaction medium	NH₃ produced in 120 min (μmol)	NH₃ produced in 60 min (μmol h⁻¹)	NH₃ produced (μmol h⁻¹ g⁻¹) (25 mg catalyst in 50 mL solution)
CT (N ₂)	DI water	53.35	26.76	53.34
DCT (N ₂)	DI water	58.00	28.00	56.00
CT (Ar)	DI water + 1 vol.% Methanol	9.73	4.86	9.72
DCT (Ar)	DI water + 1 vol.% Methanol	21.12	10.56	21.12
CT (N ₂)	DI water + 1 vol.% Methanol	68.69	34.34	68.68
DCT (N ₂)	DI water + 1 vol.% Methanol	257.45	128.72	257.44

Table S3. Comparison of N₂ fixation performance of oxygen vacancy engineered leaf-templated CaTiO₃ with other similar materials. (OVs means oxygen vacancies)

Photocatalyst	Reaction medium	Light source	NH ₃ evolved	Ref. (Year)
TiO ₂ (OVs)	10 vol% methanol in water	Simulated sunlight Visible Light	324.86 μmol g ⁻¹ h ⁻¹ 2.21 μmol g ⁻¹ h ⁻¹	¹⁶ (2020)
Hydrogenated Bi ₂ MoO ₆ (OVs)	Water and air	Simulated sunlight	1.30 mmol g ⁻¹ h ⁻¹	¹⁷ (2016)
Fe doped BiOCl (OVs)	Water	Simulated sunlight	1.02 mmol g ⁻¹ h ⁻¹	¹⁸ (2019)
BiOBr-001 (OVs)	Water	Visible Light Simulated sunlight	104.20 μmol g ⁻¹ h ⁻¹ 223.30 μmol g ⁻¹ h ⁻¹	¹⁹ (2015)
Bi ₂ MoO ₆ /OV-BiOBr	Water	Visible Light Simulated sunlight	81.0 μmol g ⁻¹ h ⁻¹ 90.70 μmol g ⁻¹ h ⁻¹	²⁰ (2019)
Bi-rich Bi ₅ O ₇ I-001 Bi ₅ O ₇ I-100	20 vol% methanol in water	Simulated sunlight	111.50 μmol L ⁻¹ h ⁻¹ 47.60 μmol L ⁻¹ h ⁻¹	²¹ (2016)
Defected Bi ₃ O ₄ Br Nanosheets	Water	Simulated sunlight	380.0 μmol g ⁻¹ h ⁻¹	²² (2019)
CaTiO ₃ (OVs)	Water 1 vol% methanol in water	Natural sunlight	56.0 μmol h ⁻¹ g ⁻¹ 236.12 μmol h ⁻¹ g ⁻¹	This work

References

1. Hohenberg, P.; Kohn, W. Inhomogeneous Electron Gas. *Physical Review* **1964**, *136*, B864-B871.
2. Kohn, W.; Sham, L. J. Self-Consistent Equations Including Exchange and Correlation Effects. *Physical Review* **1965**, *140*, A1133-A1138.
3. Kresse, G.; Furthmüller, J. Efficiency of ab-initio total energy calculations for metals and semiconductors using a plane-wave basis set. *Computational Materials Science* **1996**, *6*, 15-50.
4. Kresse, G.; Joubert, D. From ultrasoft pseudopotentials to the projector augmented-wave method. *Physical Review B* **1999**, *59*, 1758-1775.
5. Blöchl, P. E. Projector augmented-wave method. *Physical Review B* **1994**, *50*, 17953-17979.
6. Perdew, J. P.; Burke, K.; Ernzerhof, M. Generalized Gradient Approximation Made Simple. *Physical Review Letters* **1996**, *77*, 3865-3868.
7. Krukau, A. V.; Vydrov, O. A.; Izmaylov, A. F.; Scuseria, G. E. Influence of the exchange screening parameter on the performance of screened hybrid functionals. *The Journal of Chemical Physics* **2006**, *125*, 224106.
8. Pack, J. D.; Monkhorst, H. J. "Special points for Brillouin-zone integrations"---a reply. *Physical Review B* **1977**, *16*, 1748-1749.
9. Cai, J.; Cao, A.; Huang, J.; Jin, W.; Zhang, J.; Jiang, Z.; Li, X. Understanding oxygen vacancies in disorder-engineered surface and subsurface of CaTiO₃ nanosheets on photocatalytic hydrogen evolution. *Applied Catalysis B: Environmental* **2020**, *267*, 118378.
10. Tan, H.; Zhao, Z.; Zhu, W.-b.; Coker, E. N.; Li, B.; Zheng, M.; Yu, W.; Fan, H.; Sun, Z. Oxygen vacancy enhanced photocatalytic activity of perovskite SrTiO₃. *ACS Applied Materials & Interfaces* **2014**, *6*, 19184-19190.
11. Zhang, G.; Jiang, W.; Hua, S.; Zhao, H.; Zhang, L.; Sun, Z. Constructing bulk defective perovskite SrTiO₃ nanocubes for high performance photocatalysts. *Nanoscale* **2016**, *8*, 16963-16968.
12. Zhang, Y.; Xu, Z.; Li, G.; Huang, X.; Hao, W.; Bi, Y. Direct Observation of Oxygen Vacancy Self-Healing on TiO₂ Photocatalysts for Solar Water Splitting. *Angewandte Chemie* **2019**, *131*, 14367-14371.

13. Sambandam, B.; Michael, R. J. V.; Manoharan, P. T. Oxygen vacancies and intense luminescence in manganese loaded ZnO microflowers for visible light water splitting. *Nanoscale* **2015**, *7*, 13935-13942.
14. Wang, J.; Xia, Y.; Zhao, H.; Wang, G.; Xiang, L.; Xu, J.; Komarneni, S. Oxygen defects-mediated Z-scheme charge separation in g-C₃N₄/ZnO photocatalysts for enhanced visible-light degradation of 4-chlorophenol and hydrogen evolution. *Applied Catalysis B: Environmental* **2017**, *206*, 406-416.
15. Xie, Y. P.; Yang, Y.; Wang, G.; Liu, G. Oxygen vacancies promoted interfacial charge carrier transfer of CdS/ZnO heterostructure for photocatalytic hydrogen generation. *Journal of Colloid and Interface Science* **2017**, *503*, 198-204.
16. Zhang, G.; Yang, X.; He, C.; Zhang, P.; Mi, H. Constructing a tunable defect structure in TiO₂ for photocatalytic nitrogen fixation. *Journal of Materials Chemistry A* **2020**, *8*, 334-341.
17. Hao, Y.; Dong, X.; Zhai, S.; Ma, H.; Wang, X.; Zhang, X. Hydrogenated bismuth molybdate nanoframe for efficient sunlight-driven nitrogen fixation from air. *Chemistry—A European Journal* **2016**, *22*, 18722-18728.
18. Zhang, N.; Li, L.; Shao, Q.; Zhu, T.; Huang, X.; Xiao, X. Fe-Doped BiOCl Nanosheets with Light-Switchable Oxygen Vacancies for Photocatalytic Nitrogen Fixation. *ACS Applied Energy Materials* **2019**, *2*, 8394-8398.
19. Li, H.; Shang, J.; Ai, Z.; Zhang, L. Efficient visible light nitrogen fixation with BiOBr nanosheets of oxygen vacancies on the exposed {001} facets. *Journal of the American Chemical Society* **2015**, *137*, 6393-6399.
20. Xue, X.; Chen, R.; Yan, C.; Hu, Y.; Zhang, W.; Yang, S.; Ma, L.; Zhu, G.; Jin, Z. Efficient photocatalytic nitrogen fixation under ambient conditions enabled by the heterojunctions of n-type Bi₂MoO₆ and oxygen-vacancy-rich p-type BiOBr. *Nanoscale* **2019**, *11*, 10439-10445.
21. Bai, Y.; Ye, L.; Chen, T.; Wang, L.; Shi, X.; Zhang, X.; Chen, D. Facet-dependent photocatalytic N₂ fixation of bismuth-rich Bi₅O₇I nanosheets. *ACS Applied Materials & Interfaces* **2016**, *8*, 27661-27668.
22. Di, J.; Xia, J.; Chisholm, M. F.; Zhong, J.; Chen, C.; Cao, X.; Dong, F.; Chi, Z.; Chen, H.; Weng, Y. X. Defect-Tailoring Mediated Electron–Hole Separation in Single-Unit-Cell Bi₃O₄Br Nanosheets for Boosting Photocatalytic Hydrogen Evolution and Nitrogen Fixation. *Advanced Materials* **2019**, *31*, 1807576.